

Alpha-Particle Gas-Pressure Sensor

M. G. Buehler, L. D. Bell, and M. H. Hecht
Microdevices Laboratory
Jet Propulsion Laboratory
California Institute of Technology
Pasadena, CA, 91109

ABSTRACT: An approximate model was developed to establish design curves for the saturation region and a more complete model developed to characterize the current-voltage curves for an alpha-particle pressure sensor. A simple two-parameter current-voltage expression was developed to describe the dependence of the ion current on pressure. The parameters are the saturation-current pressure coefficient and μ/D , the ion mobility/diffusion coefficient. The sensor is useful in the pressure range between 0.1 and 1000 mb using a 1- μ Ci ^{241}Am source. Experimental results, taken between 1 and 200 mb, show the sensor operates with an anode voltage of 5 V and a sensitivity of 20 fA/mb in nitrogen.

1. INTRODUCTION: This work is motivated by the need to measure the Martian pressure which is seen as critical to modeling its atmosphere [1]. The atmospheric model requires many pressure sensors distributed over the surface of Mars thus providing a measure of the pressure field. The deployment of such a network of pressure sensors requires that sensors survive a hard landing of about 7400 g's, be small and light, and operate at low power and low temperature of 150 K. The prototype device described here is the first pressure gage to operate from a 5 volt supply. This attribute is very important for low power operation.

The use of radioactive isotopes for generating ion currents to measure pressure was first demonstrated in the late 1940s by Downing and Mellen [2] and Dick, Falk-Vairant and Rossel [3]. The early gages operated at high voltages (sometimes in the kilovolt range), used rather large ion sources (sometimes in the Ci range), and had sensitivities in excess of a pA/mb [4].

The prototype sensors, fabricated in this study, were operated with a low source strength (1 μ Ci) and low voltage (<5 V), the size of the chamber can be small; the

prototype has a linear dimension of 2 cm. Since the gage has no moving parts or suspended filaments, it is robust. These characteristics make this gage suitable for transport to the surface of Mars via a hard lander where the gage will operation from 150 to 325K and from 3 to 15 mb in a CO₂ atmosphere.

2. SENSOR OPERATION: This detector utilizes the ability of alpha particles to ionize gas molecules which subsequently drift in an electric field to a cathode that is connected to a current detection device. The configuration for this pressure sensor is shown in Fig. 1. In this arrangement, the alpha source is grounded anti the anode is held at a positive potential. The cathode is connected directly to the input pin of an operational amplifier. Such an arrangement is intended to allow the measurement of sub pA currents.

The measurement principle is illustrated graphically in Fig. 2, which shows the reduction in alpha particle energy as the alphas traverse the ionization chamber filled with air at pressures ranging from 100 to 1000 mb. The chamber consists of an alpha particle source located at $x = 0$ and a harrier (anode in this case) located at $x = H = 50$ mm. The barrier can be a physical barrier such as metal plate or it can be an electric field. This point will discussed later in the experiment section.

As the alphas traverse the chamber, they ionize the gas, creating positively charged ions. The average energy lost by an alpha particle in ionizing a gas molecule is about 30 eV/ion pair. Literature values for the average energy for a number of gasses is listed in Table 1. This means that a 3 MeV alpha particle can create 100,000 ions.

Another feature of the detector is the separation of the positively charged ions from the electrons by the electric field in the chamber. Positively charged ions drift in the direction of the electric field anti electrons drift in the direction opposite to the electric field. Both ions or electrons may be measured by changing the sign of the potential on the anode relative to the cathode.

3. DESIGN CURVE DERIVATION: in this section a set of curves are developed to guide the design and operation of the prcls.sure sensor. "These curves are based on the assumption that the sensor is operated in saturation where the electric field is high enough so that the positively charged ions do not recombine before the ions reach the cathode. The saturation region is determined as that portion of the curve where the ion current does not depend on the anode voltage, in saturation, the ion current measured at the cathode is given by:

$$I = q(E_1 \cdot E_2)N_C \cdot S/W \quad (1)$$

where q is the electronic charge, E_1 is the initial alpha particle energy as it enters the chamber, E_2 is the alpha energy at the barrier, S is the number of alpha particle disintegrations/ $\mu\text{Ci/s}$ or $3.7 \times 10^4/\mu\text{Ci}\cdot\text{s}$, N_C is the alpha source activity in μCi , and W is the average alpha energy lost per ion pair created.

The key feature of this pressure sensor is that the alpha particles must reach the barrier with a finite amount of energy; that is, at H , E_2 cannot be zero. If the alphas reach end-of-range before reaching the barrier, then all their energy is deposited in the chamber and the ion current will be constant independent of the pressure. This is illustrated in Fig. 2 for the 800 and 1000 mb pressure curves. In order to measure these pressures, the barrier shown at 50 mm must be placed at a distance no greater than about 35 mm.

The functional dependence of the ion current is derived by approximating the alpha range-energy curve for alphas in air and CO_2 [7] is shown in Fig. 3 for standard temperature and pressure (STP). The alpha range at STP is R_0 . In the following analysis, the range-energy curve was approximated using:

$$E_i/E_f = (R_i/R_f)^n \quad (2)$$

where n , E_f and R_f are fitting parameters, E_i is the alpha energy, and R_i is the alpha range. As determined from Fig. 3, values for n range from 0.5 to 1.

The energy difference found in Eq. 1 is analyzed using Eq. 2:

$$E_1 - E_2 = E_f(R_1/R_f)^n - E_f(R_2/R_f)^n \quad (3)$$

where R_1 and R_2 are the ranges for alphas with energies E_1 and E_2 , respectively. Since $R_2 = R_1 - H$, Eq. 3 simplifies for $H \ll R_1$ to:

$$E_1 - E_2 = n \cdot E_1 \cdot H / R_1 \quad (4)$$

The ionization gage is a densitometer the output of which varies with gas species in the chamber, gas temperature and gas pressure. The Bragg Kleeman rule [8] relates the alpha range, R , to the gas density, ρ , as follows:

$$R_1/R_{10} = \rho_0/\rho \quad (5)$$

where R_{10} is the alpha range and ρ_0 is the gas density at STP. Thus, the energy difference is:

$$E_1 - E_2 = n \cdot E_1 \cdot H \cdot \rho / (R_{10} \cdot \rho_0) \quad (6)$$

This equation shows that the energy difference is proportional to gas density, ρ . The density is related to temperature, T , and pressure, P , through the ideal gas law expressed relative the standard temperature and pressure:

$$\rho/\rho_0 = (P/P_0)(T_0/T) \quad (7)$$

where P_0 and T_0 are the temperature and pressure, respectively at STP where $P_0 = 1013.25$ mb and $T_0 = 273.15$ K. The approximate ion current expression in saturation is:

$$I = q \cdot n \cdot E_1 \cdot S \cdot N_C \cdot H \cdot P \cdot T_0 / (W \cdot R_{10} \cdot P_0 \cdot T) \quad (8)$$

This expression indicates that the ion current increases linearly with N_C , H , and P and inversely with T . It also indicates that the ion current is species sensitive through the R_{10} and n parameters. The R_{10} ratio for air and CO_2 is about 1.6 and is the inverse of the ratio of the respective gas densities listed in Table 1.

4. DESIGN CURVES: The normalized ion current-pressure design curves are presented in Figs. 4 to 9 where the parameters E_1 , H , and T are varied about the target values $E_1 = 5$ MeV, $H = 20$ mm, and $T = 225$ K. The design curves were calculated using Eq. 1 where $W = 32.9$ eV/pair, $q = 1.6 \times 10^{-19}$ C, and $S = 3.7 \times 10^4 / \mu\text{Ci}\cdot\text{s}$.

The energy difference, $E_1 - E_2$, was determined as follows. First, E_1 was chosen and R_{10} determined from an approximate alpha particle presented in the Appendix. Then the range was corrected to the specified T and P using the combination of Eqs. 5 and 7:

$$R_1 = R_{10}(P/P_0)(T_0/T) \quad (9)$$

Then R_2 was calculated from:

$$R_2 = R_1 - H \quad (10)$$

and transformed to STP using:

$$R_{20} = R_2(P_0/P)(T/T_0) \quad (11)$$

to allow the calculation of E_2 using the inverse of the approximation presented in the Appendix. Finally, the current was calculated using Eq. 1.

An overview of the design space is shown in Fig. 4 where the upper and lower bound for each parameter is used. This figure indicates that the ion current increases linearly with pressure up to the point where the alphas reach end-of-range before encountering the barrier (anode). This is indicated by the saturation behavior shown in the figure. When this condition is reached, pressure measurements are not possible.

In Figs 5 through 7 an analysis is presented of the influence of H , T and E_1 on the ion current. In Fig. 5, the current-pressure curves are seen to increase linearly with the height of the chamber, H . The data indicates that a larger chamber is needed at lower pressures to obtain more ion current. For low pressures, a chamber several centimeters in extent is desirable. For higher pressures, the chamber could be only several millimeters in extent and this would allow the construction of very small pressure sensors.

The temperature dependence of the ion current-pressure curves, shown in Fig. 6, indicates that the temperature does not affect the ion current as strongly as H . Thus, temperature has a weaker impact on the chamber design.

The energy dependence of the current-pressure curves is shown in Fig. 7. This figure indicates that the ion current depends strongly on the alpha particle energy. When the curves saturate or appear horizontal, the alpha particles reach their end-of-range before striking the anode. As mentioned before, no pressure measurement is possible in this region. The ion current dependence on alpha energy is explored further in Fig. 8. These results indicate that the ion current has a maximum at certain alpha energies. These curves are important in mass producing these units; they indicate that individual units must be calibrated since source variations are typically 10 percent.

5. EXPERIMENTAL. RESULTS: Experimental results were obtained using an ionization gage as depicted schematically in Fig. 1. The height of the chamber is $H = 20$ mm. A 1- μ Ci alpha particle ^{241}Am source, was placed beneath the cathode. The anode was biased both positively and negatively with respect to the cathode. The cathode was connected to an CIPA111 operational amplifier.

The chamber pressure was measured with a Granville-Phillips Convection. During measurements, the chamber was filled with nitrogen.

The current-voltage curves for the sensor are shown in Fig. 9 for both positive and negative biases on the anode. The current is due to positive ions when the anode is positive and the current is due to electrons when the anode is negative. The offset at zero volts is probably due to stray fields caused by surface charging of insulators in the ionization chamber. The curves were observed to saturate at higher voltages for positive bias than for negative bias.

The ion current-pressure curve is shown in Fig. 10 for an anode voltage of $V_a = 5V$. The fit to the data indicates that the current sensitivity to pressure is 18.8 fA/mb. The pressure range shown in Fig. 10 is the range expected for the Martian environment.

6. ION CURRENT MODEL: The model used above was limited to the saturation region in order to describe the current-pressure behavior. In this section a model is developed for the ion current-voltage behavior between the linear and saturation regions. A comprehensive model for the ion current-voltage behavior is available [9] but its solution is numerical. In this effort, an analytical one-dimensional solution is derived that reveals the influence of physical parameters on the ion chamber current-voltage behavior. This problem is similar to the drift and diffusion of minority carriers in a uniformly illuminated semiconductor described by Sze [10].

In this model the operation of the chamber is assumed to be in or near the high field saturation region where the electron concentration can be neglected since the electron mobility is about 1000 times larger than for ions. The model is based on a planar geometry chamber where the charge generation is uniform and an electric field is imposed along the positive x-axis of the chamber. The chamber has uniform recombination and the recombination process is proportional to the positive ion density, p ($\#/cm^3$). The continuity equation for the current density, J (A/cm^2), is:

$$V \cdot J = q(G - p/\tau) \quad (12)$$

where τ is the recombination lifetime (s), q is the electronic charge (C), and G is the ion generation rate ($\#/cm^3 \cdot s$). The transport through the chamber is governed by an electric field drift component and by a diffusion component so the ion current density is:

$$J = q\mu\mathcal{E} \cdot qDdp/dx \quad (13)$$

where μ is the ion mobility ($\text{cm}^2/\text{V}\cdot\text{s}$), \mathcal{E} is the electric field (V/cm), and D is the diffusion coefficient (cm^2/s). For this planar geometry, $\mathcal{E} = V_a/H$. The combination of Eqs. 12 and 13 leads to the differential equation for the chamber:

$$-D \cdot d^2p/dx^2 + \mu \mathcal{E} \cdot dp/dx + p/\tau = G \quad (14)$$

The solution for p is the sum of the steady state solution and the transient solution and the boundary conditions where $p = 0$ at $x = 0$ and $x = H$. The ion density is:

$$p = G\tau [1 + K_1 \cdot \exp(r_1 x) + K_2 \cdot \exp(r_2 x)] \quad (15)$$

where R_1 , R_2 , K_1 , and K_2 are listed in Table 2, $L = \sqrt{(D \cdot \tau)}$ is the diffusion length, $M = p/D$ is the Einstein relation, and H is the height of the chamber.

The normalized ion density is shown graphically in Figs. 11 and 12 for various values of L' and \mathcal{E}' where the normalized diffusion length is $L' = \sqrt{(D \cdot \tau)}/H$, the normalized electric field is $\mathcal{E}' = \mu V_a/D$, and the normalized distance across the chamber is $X' = x/H$. An inspection of Fig. 11 reveals how the normalized electric field influences the ions as they traverse the chamber between the anode located at $X' = 0$ and cathode located at $X' = 1$. An inspection of Fig. 12 reveals how the normalized diffusion length affects the ions as they traverse the chamber. Notice that the current flow is dominated by drift in the center of the chamber and by diffusion at the edges of the chamber. This observation will be used later to explain the experimental results.

The current that can be extracted from the chamber at the cathode is given by the slope of the concentration at the cathode. The current density at the cathode was derived by evaluating Eq. 15 at $x = H$ where $p = 0$:

$$J = -qDdp/dx|_{x=H} = -qGL^2(\mu \mathcal{E}/2D) \cdot [s_1 K_1 \exp(r_1 H) + s_2 K_2 \exp(r_2 H)] \quad (22)$$

where s_1 and s_2 are listed in Table 2. The current-voltage curves, shown in Fig. 13, indicate how recombination affects the curves through the L' parameter. The curves do not intersect $J' = J/qGH = 0$ at $\mathcal{E}' = 0$ because of the simplifying assumption that the electron density is negligible.

Further analysis of the current-voltage data presented in Fig. 9 is now possible. The simplification of Eq. 22 as \mathcal{E}' approaches infinity leads to:

$$1/I = (1/I_s)[1 + 1/(M \cdot V_a)] \quad (23)$$

where $M = p/D$, $I_s = qGAH$ is the saturation ion current and A is the area of the chamber normal to the direction of the electric field. The form of this equation was also used to analyze other ion chamber data [1 1].

The pressure dependence of each parameter was introduced into Eq. 23 using the work of vonEngel [12]. The pressure dependence of the saturation current is:

$$I_s = K_g \cdot P \quad (24)$$

where K_g is the saturation-current pressure coefficient. The pressure dependence of the ion mobility is:

$$\mu = K_m/P \quad (25)$$

where K_m is the mobility pressure coefficient. The pressure dependence of the diffusion coefficient is:

$$D = K_d/p \quad (26)$$

where K_d is the diffusion-coefficient pressure coefficient. The substitution of Eqs. 24 to 26 into Eq. 23 leads to the fitting equation:

$$P/I = [1/K_g] + [1/(M \cdot K_g)]/V_a \quad (27)$$

The current-voltage characteristic shown in Fig. 9 is replotted in Fig. 14. The plotted voltage is the measured voltage minus an offset voltage found from Fig. 9 at $I = 0$. After each curve in Fig. 14 was fitted with Eq. 27, the K_g and M parameters were extracted and are listed in Table 3. The pressure dependence of these parameter is shown graphically in Fig. 15.

In Fig. 14, notice that the curves converge to a single value at $I/V_a = 0$ which is I/K_g . As seen from Table 3, the average value for K_g is 22.4 fA/mb which is close to the value of 18.8 fA/mb listed in Fig. 10. As seen in Fig. 15, the K_g parameter has no pressure dependence. This means that the ion saturation current is well described by Eq. 24.

According to Eqs. 25 and 26, p/D should not have a pressure dependence, But as seen in Fig. 15, μ/D has a pressure dependence described by:

$$M = \mu/D = K_m \cdot P^{-m} \quad (29)$$

where $K_m = 7.927$ is the Einstein-relation pressure coefficient and $m = 0.343$ is the pressure exponent. As seen in Table 3, values for μ/D are between 1 and 3 $1/V$

$$\log_{10}R_0 = n_0 + n_1 \cdot \log_{10}E_1 + n_2 \cdot (\log_{10}E_1)^2 + n_3 \cdot (\log_{10}E_1)^3 \quad (31)$$

The n-coefficient for alphas in air are shown in Fig. 17. The inverse equation is also needed in the analysis and the coefficients for this equation were found by solving the cubic equation [13]. The p- and q-coefficients for the inverse cubic are also shown in Fig. 17.

9. ACKNOWLEDGMENT:

The research described in this paper was performed by the Center for Space Microelectronics Technology, Jet Propulsion Laboratory, California Institute of Technology, and was sponsored by the National Aeronautics and Space Administration, Office of Space Access and Technology. File: PRES5C25.DOC

10. REFERENCES:

1. C. Leovy, "Exploration of the Atmosphere and Climate System of Mars," pp. 35-45 in K. Szego, ed. *The Environmental Model of Mars*, Pergamon Press (Oxford, England, 1991)
2. J. R. Downing and G. Mellen, "A Sensitive Vacuum Gauge with Linear Response," *The Review of Scientific Instruments*, Vol. 17, 218-223 (1946).
3. L. Dick, P. Falk-Vairant, and J. Rossel, "Travail l'ionisation, effets de recombinaison et pourvoir d'arret de quelques gaz pour les particles α " *J. Helv. Phys. Acts*, Vol. 20, 357-370 (1947).
4. A. Berman, "A Comprehensive Study of Ionization Gauges Using Radioactive Isotopes," *Vacuum*, Vol. 25, 51-56 (1974).
5. T. E. Bortner and G. S. Hurst, *Phys. Rev.*, Vol. 93, 1236 (1954),
6. J. Sharpe, *Nuclear Radiation Detectors*, John Wiley & Sons, Inc. (London, 1964).
7. J. F. Ziegler, J. P. Biersack, and U. Littmark, *The Stopping and Range of Ions in Solids*, Pergmon Press (New York, N. Y., 1985)
8. N. Tsoulfanidis, *Measurement and Defection of Radiation*, Hemisphere Publications Corp. (New York, N. Y., 1983)

9. F. Hajnal and J. Pane, "Calculated Saturation Curves and Ion Densities of Ionization Chambers," IEEE Trans. on Nuclear Science, Vol. NS-25, 550-552 (1978).
10. S M. Sze, *Physics of Semiconductor Devices*, J. Wiley and Sons, pp. 50-57 (New York, 1981)
11. S. M. Mustafa and K. Mahesh, "Criterion for Determining Saturation Currents in Parallel Plate Ionization Chambers," Nuclear Instruments and Methods, Vol. 150, 549-553 (1978).
12. A von Engel, *Ionized Gases*, American Institute of Physics Press (New York, 1994).
13. M. Abramowitz and I. A. Stegun, Eds., *Handbook of Mathematical Functions*, Dover Publications, Inc. (New York, N. Y., 1972).

Table 1. Critical Parameters for Selected Gases

Gas	ENERGY, W eV/ion pair	REF.	ION MOBILITY, μ $\text{cm}^2\cdot\text{atm}/\text{V}\cdot\text{s}$	REF.	DENSITY at STP, g/cc
Air	35.0	[5]	--	-	1.293 E-3
' 2	32.2	[5]	--	--	--
' 2	36.3	[5]	2..7	[6]	--
CO*	34.3	[5]	--	--	1.977 E-3

Table 2. Equation Coefficients

COEFFICIENT	Eq.
$K_1 = -[1 - \exp(r_2 H)] / [\exp(r_1 H) - \exp(r_2 H)]$	(6)
$K_2 = [1 - \exp(r_1 H)] / [\exp(r_1 H) - \exp(r_2 H)]$	(7)
$r_1 = s_1 \cdot M \varepsilon / 2$	(18)
$r_2 = s_2 \cdot M \varepsilon / 2$	(19)
$s_1 = 1 + \sqrt{[1 + (2/LM\varepsilon)^2]}$	(20)
$s_2 = 1 - \sqrt{[1 + (2/LM\varepsilon)^2]}$	(21)

Table 3. Parameters extracted from the data of Fig. 14.

DATA SYMBOL	P mb	K _g fA/mb	p/D 1/V
P4	199.95	22.85	1.21
P3	109.31	23.58	1.75
P2	53.99	21.86	1.97
P1	26.66	21.32	2.53

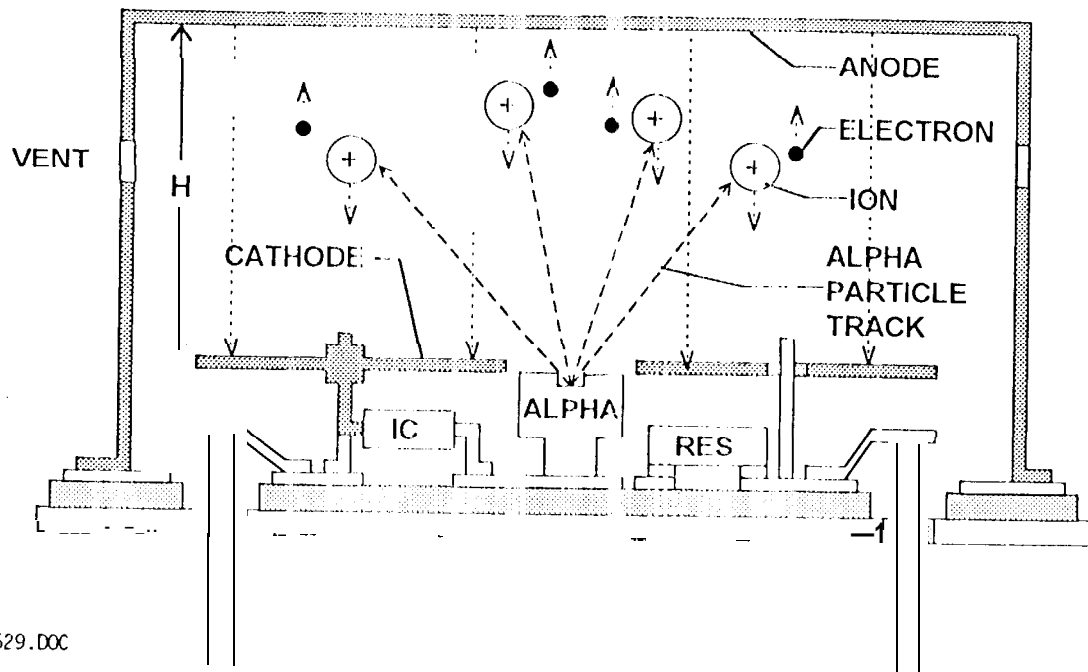


Figure 1. Configuration of the alpha-particle gas-pressure sensor where the distance between the anode anti cathode is t-i.

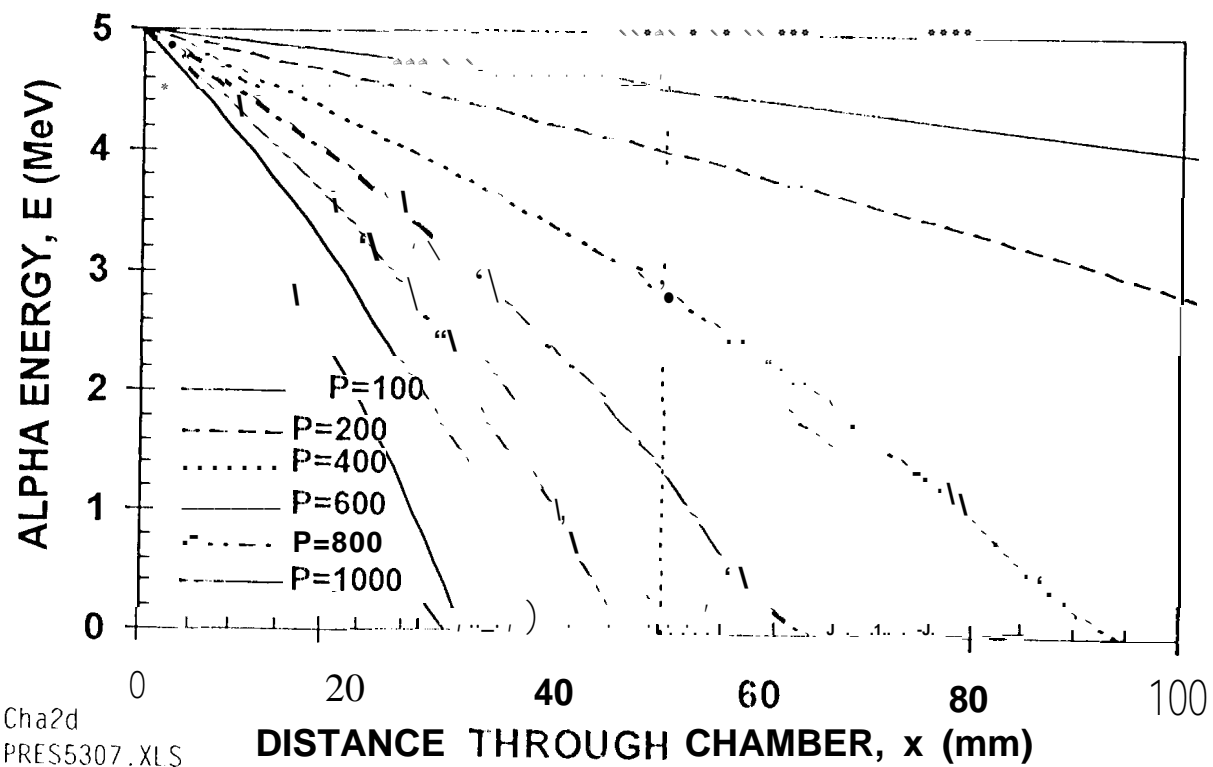


Figure 2. Alpha-particle energy as a function of the distance traversed in air and calculated for several pressures P in mb. The curves were calculated for $E_i = 5$ MeV and $T = 300$ K. The dotted line indicates the location of the anode at $H = 50$ mm. For this location only pressures less than 800 mb can be measured,

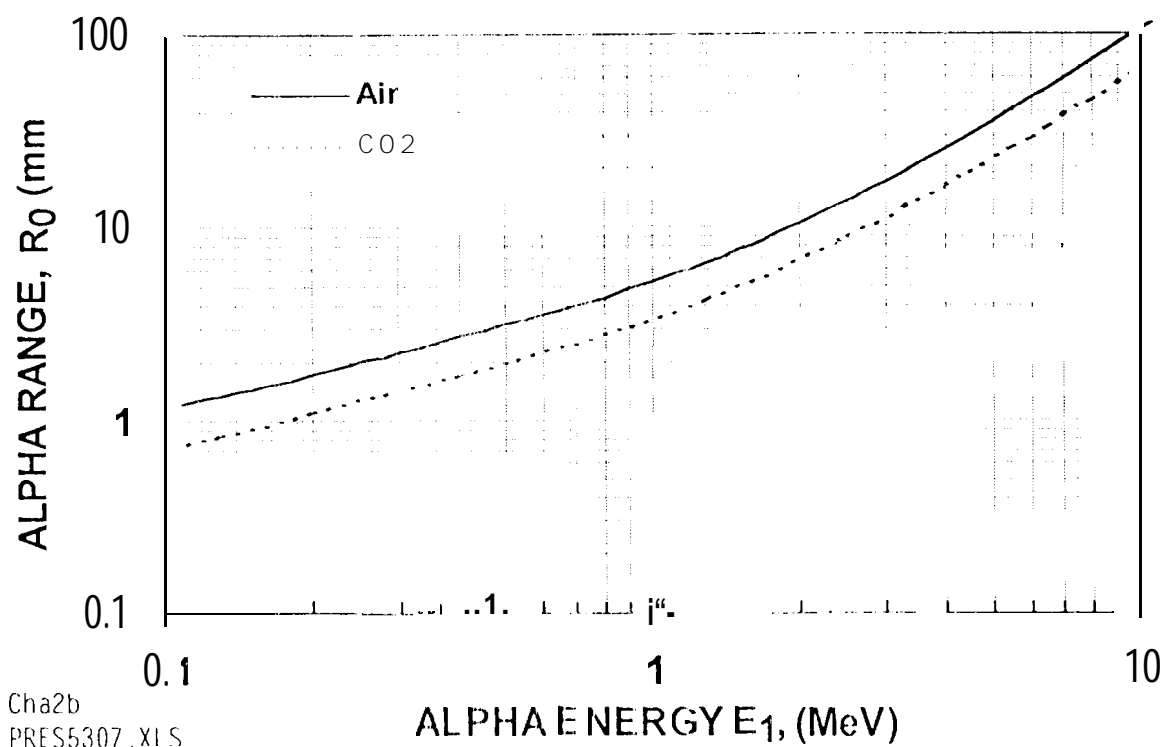


Figure 3. Alpha-particle range-energy curves for air and CO₂ at STP.

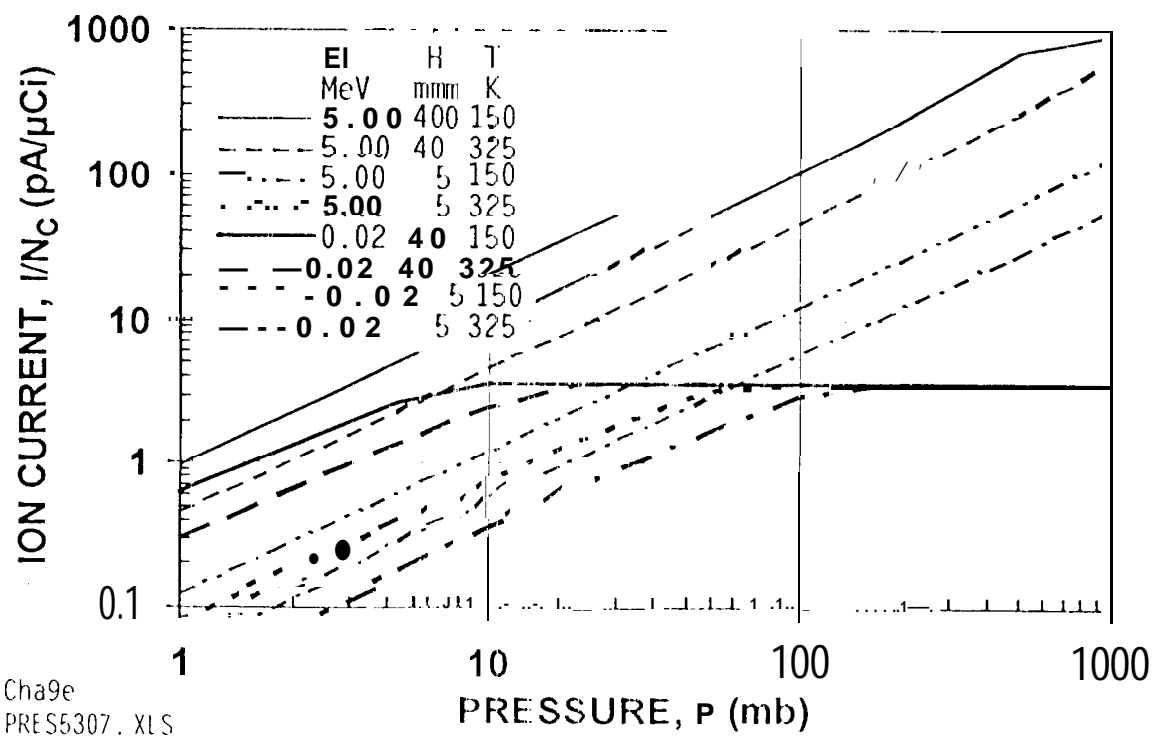


Figure 4. Calculated alpha-particle ion currents in air for various EI, H, and T values, Current saturation occurs when the alphas reach end-of-range before traversing the chamber. In this case no pressure measurement is possible.

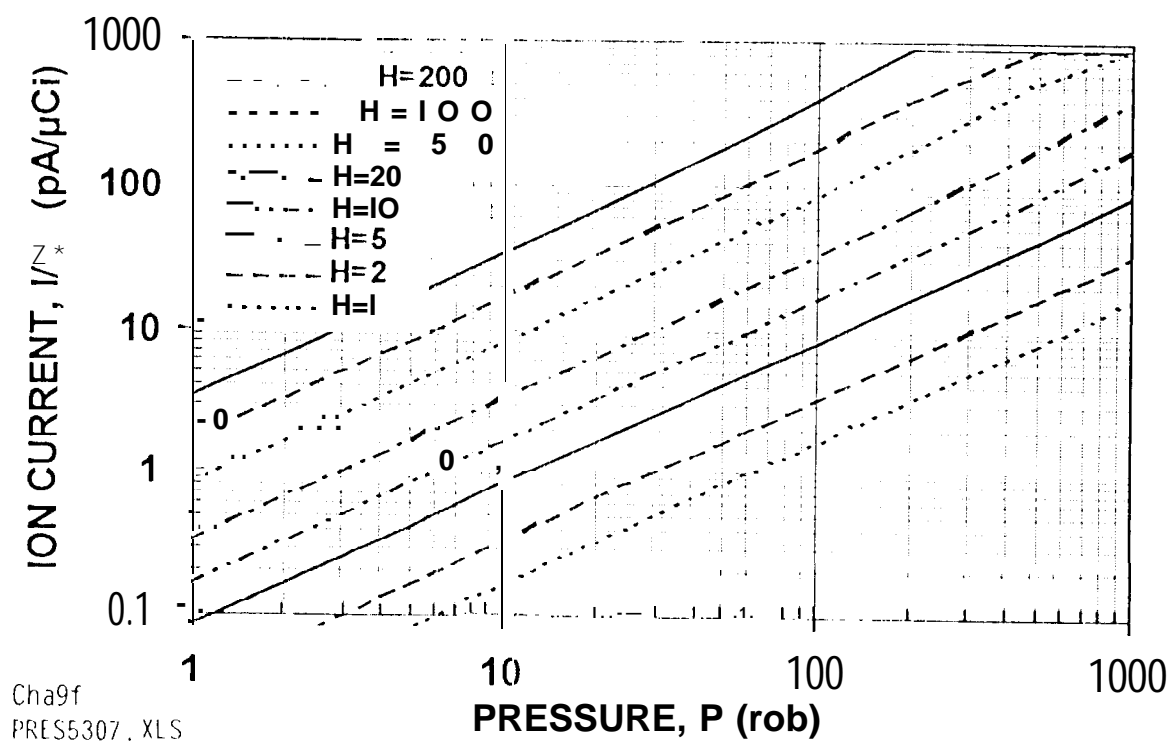


Figure 5. Calculated alpha-particle ion currents in air for various anode-cathode distances H in mm at $E_1 = 5$ MeV and $T = 225$ K.

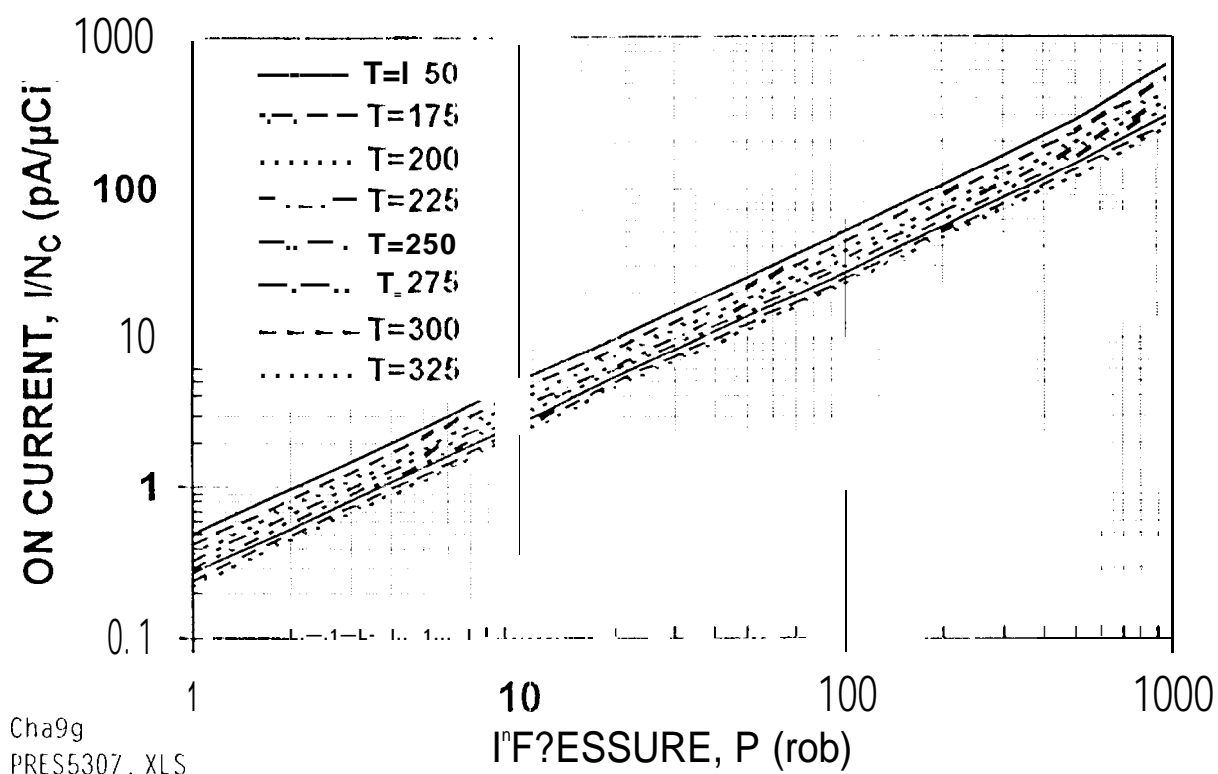


Figure 6. Calculated alpha-particle ion currents in air for various temperatures T in K at $E_1 = 5$ MeV and $H = 20$ mm.

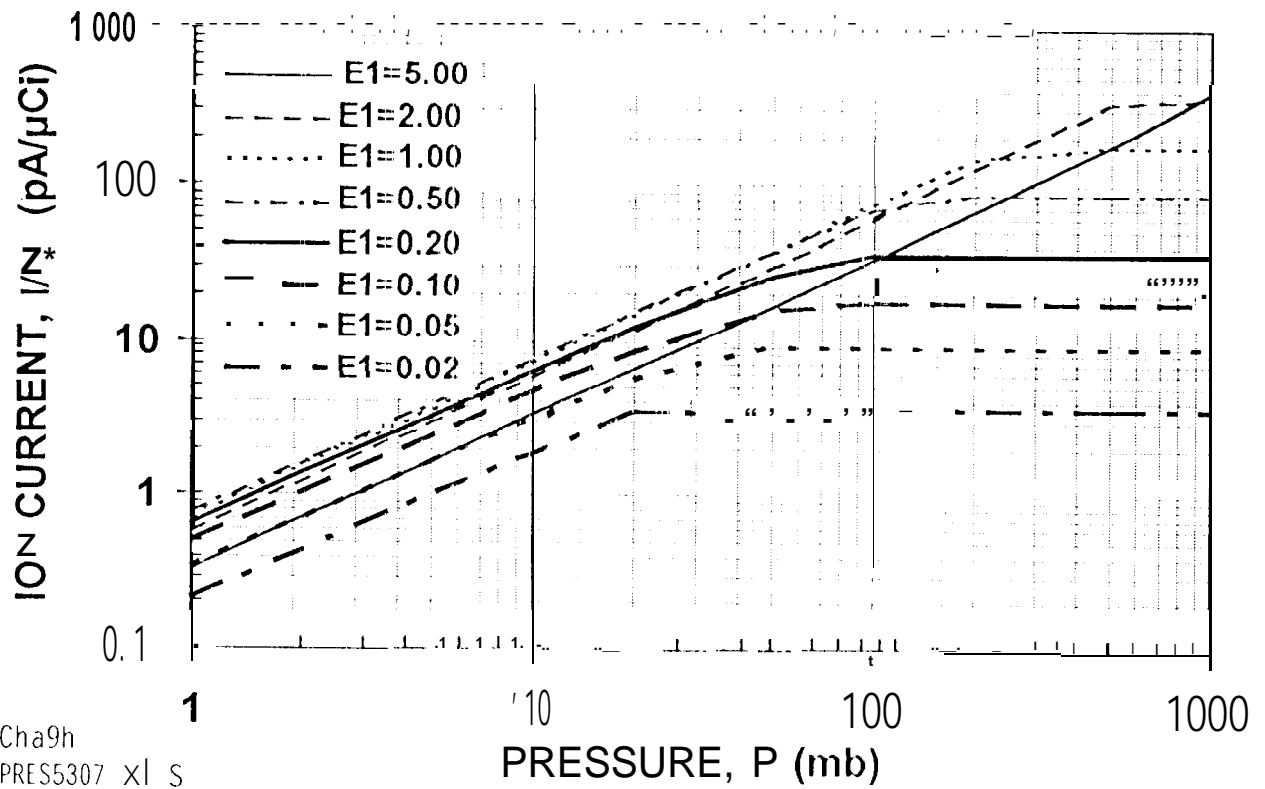


Figure 7. Calculated alpha-particle ion currents in air for various alpha particle energies E_1 in MeV at $T = 225$ K and $H = 20$ mm.

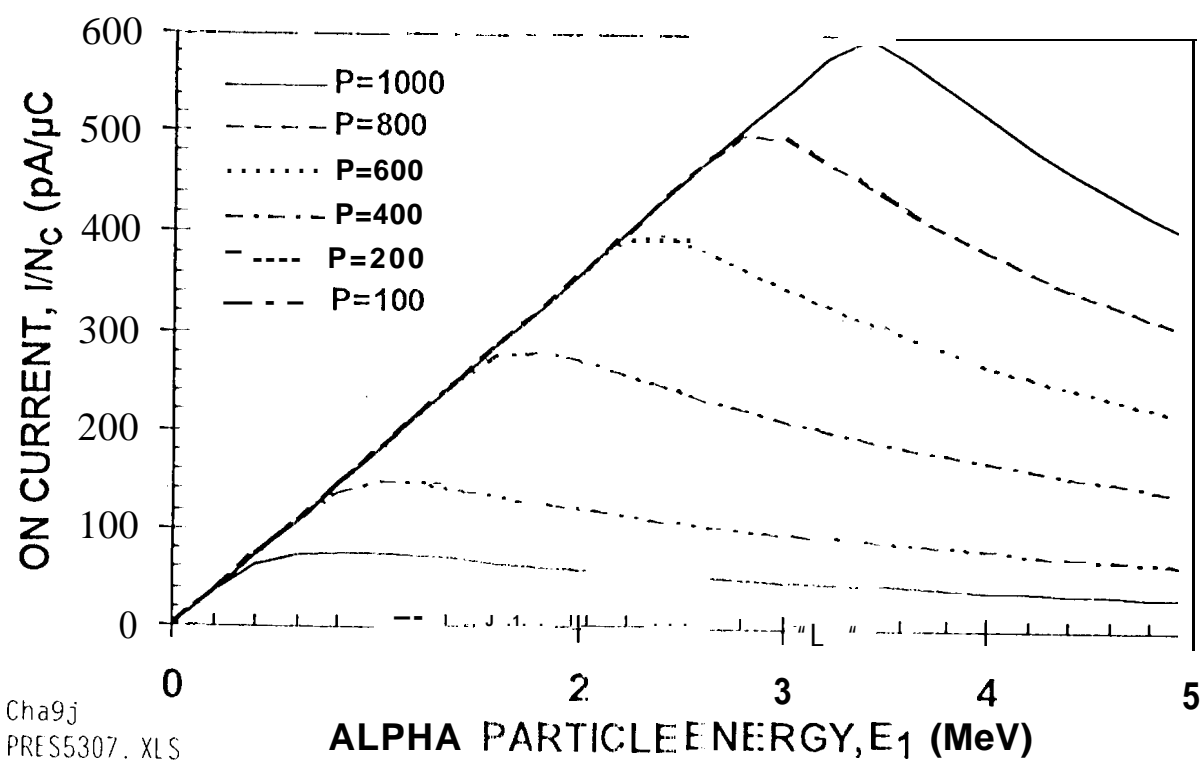


Figure 8. Calculated ion current alpha-particle energy dependence in air at various pressures P in mb at $H \approx 20$ mm and $T = 225$ K.

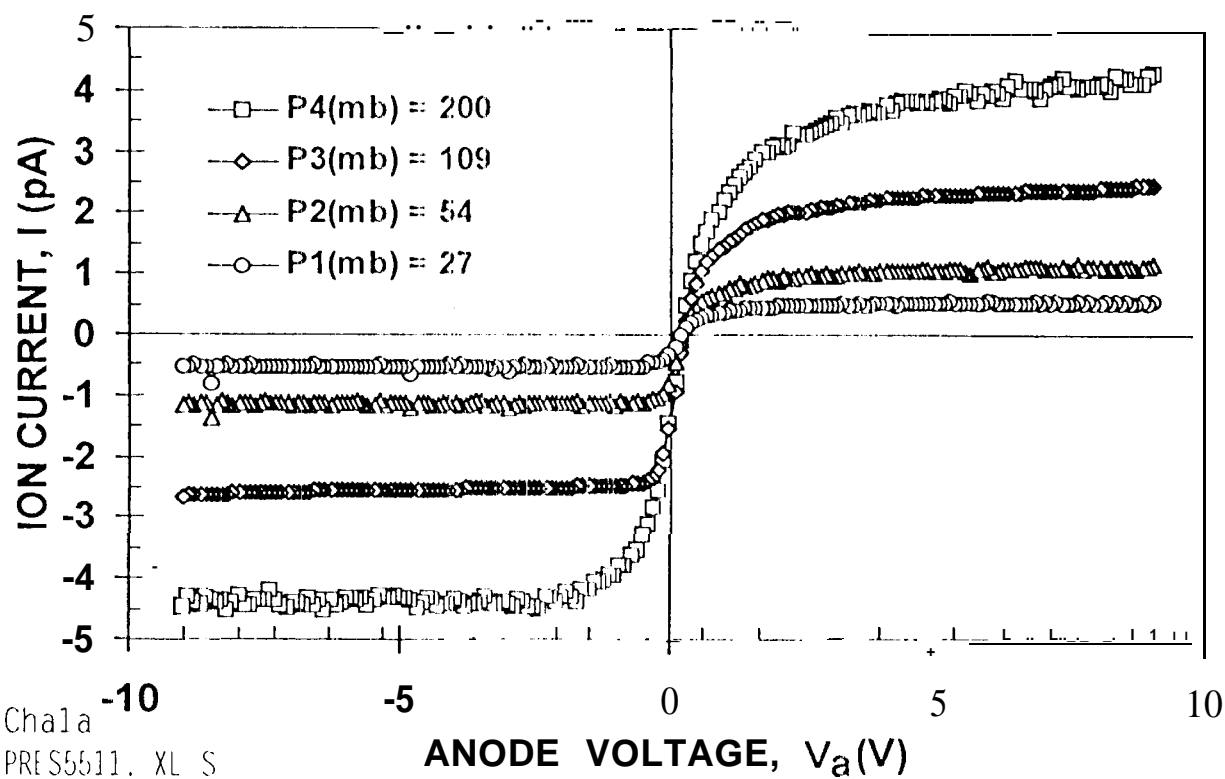


Figure 9. Experimental current-voltage gas pressure characteristics showing the saturation region at higher voltages. Note this chamber can be operated in saturation at 5 V.

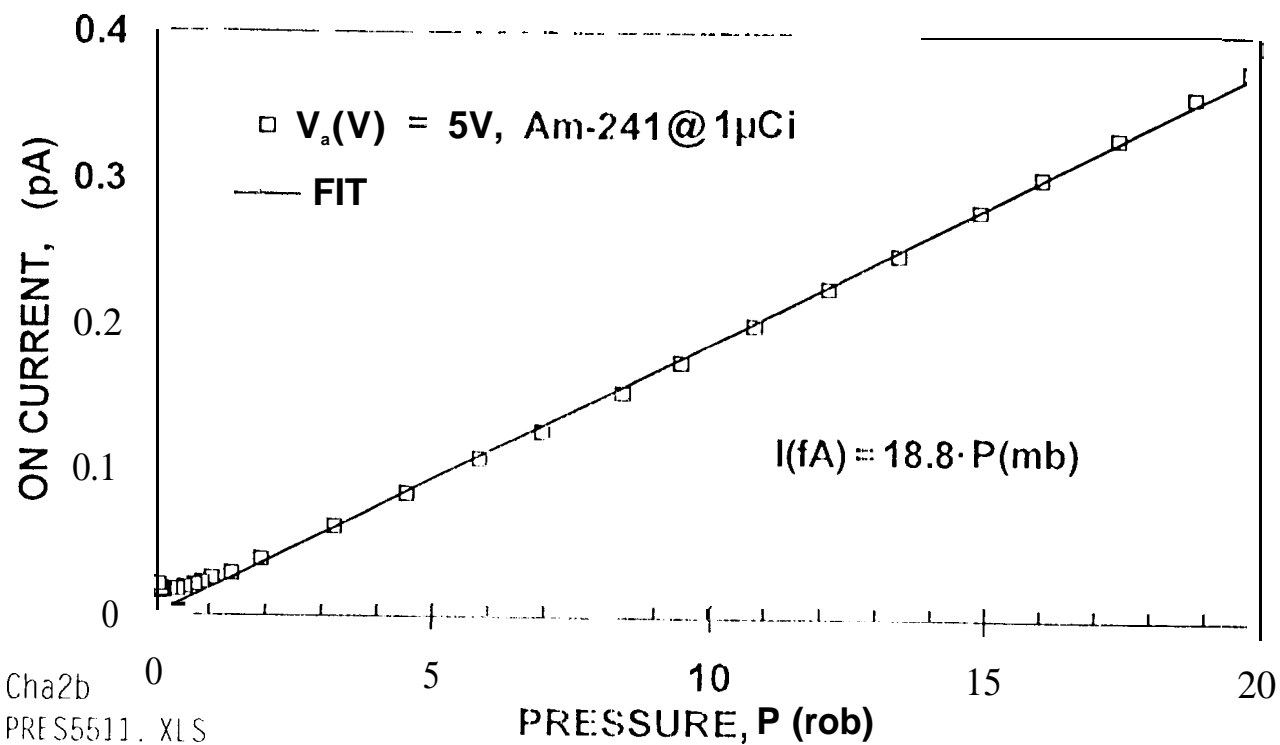


Figure 10. Experimental data verifying the linear dependence between the ion current and the pressure for $E_1 = 5$ MeV, $T = 300$ K, anti $V_a = 5$ V.

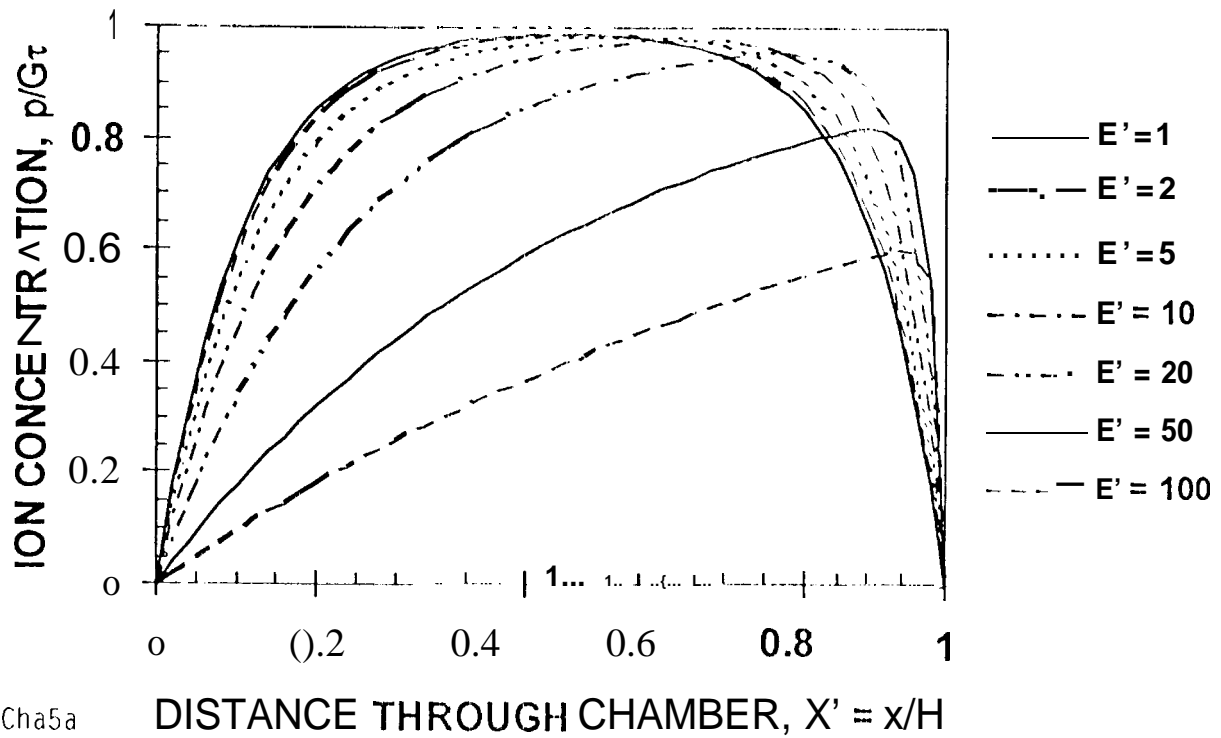
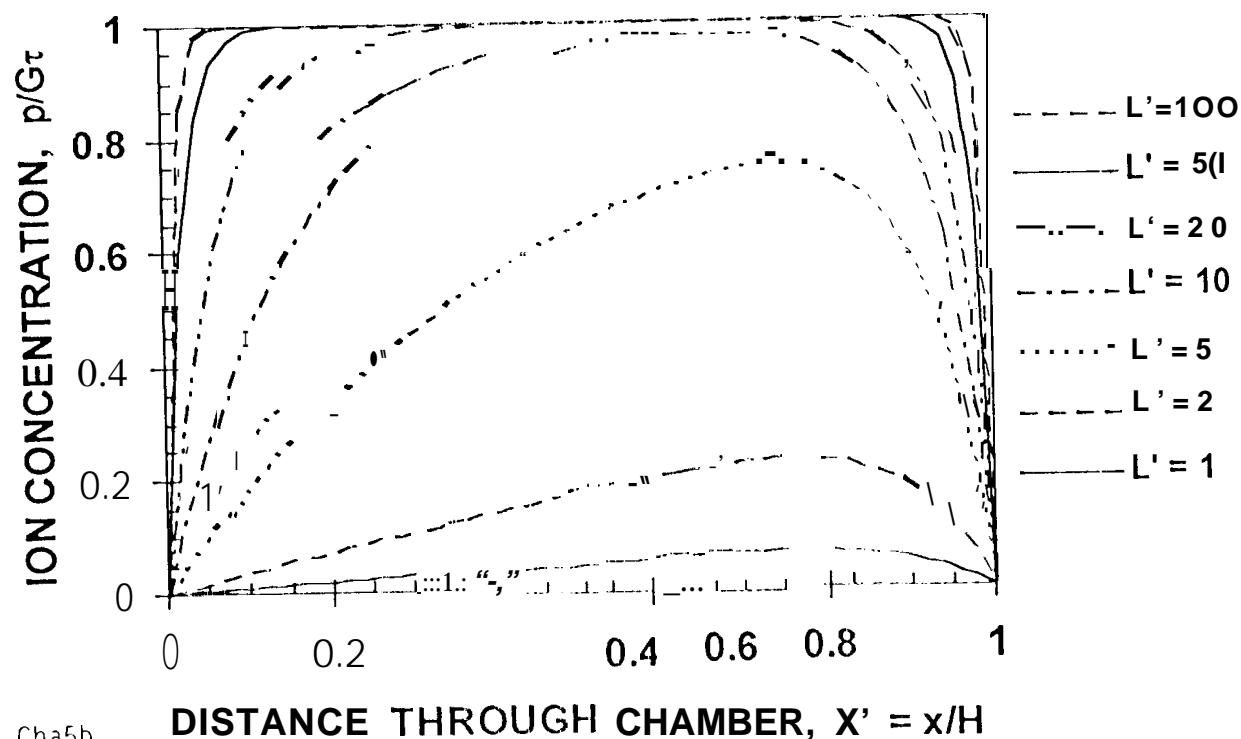


Figure 11. Calculated ion density across the chamber where the anode is located at $X' = 0$ and the cathode at $X' = 1$ for $1 \leq E' \leq 100$ and various E' values. The chart shows the influence of the electric field in drifting ions to the cathode,



Cha5b
PRES5319.XLS

Figure 12. Calculated ion density across the chamber where the anode is at $X' = 0$ and the cathode at $X' = 1$ for $\mathcal{E}' = 10$ and various L' values. The chart shows that for small L' values, recombination reduces the charge in the chamber which reduces the output current,

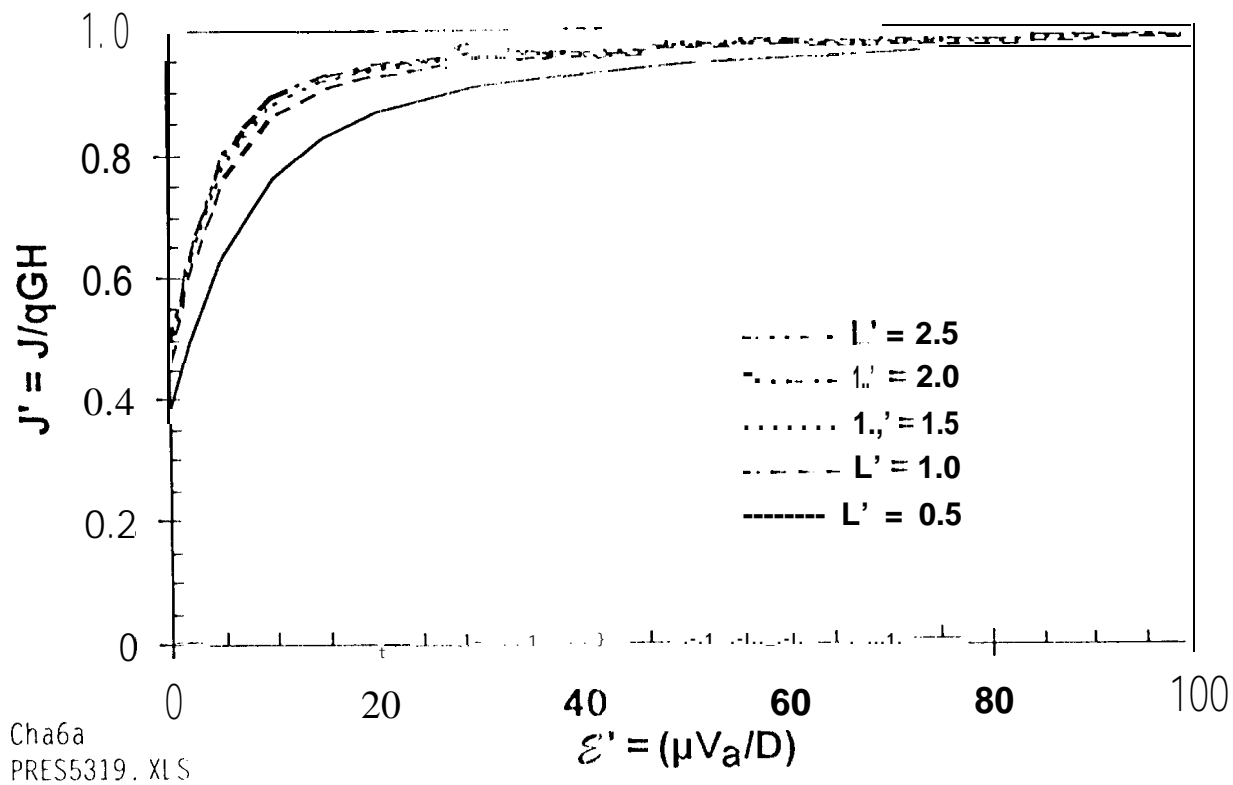


Figure 13. Normalized ion current for various ε' and L' values.

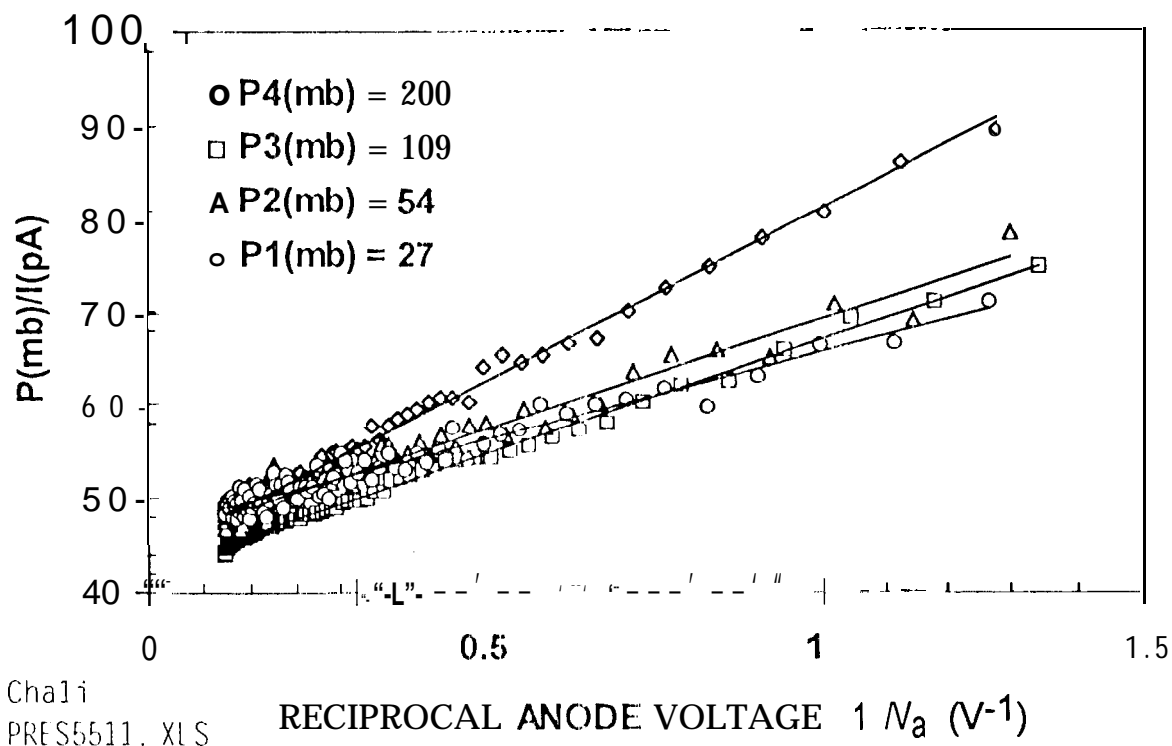


Figure 14, Ion current from Fig.9 replotted to allow an analysis of the saturation region.

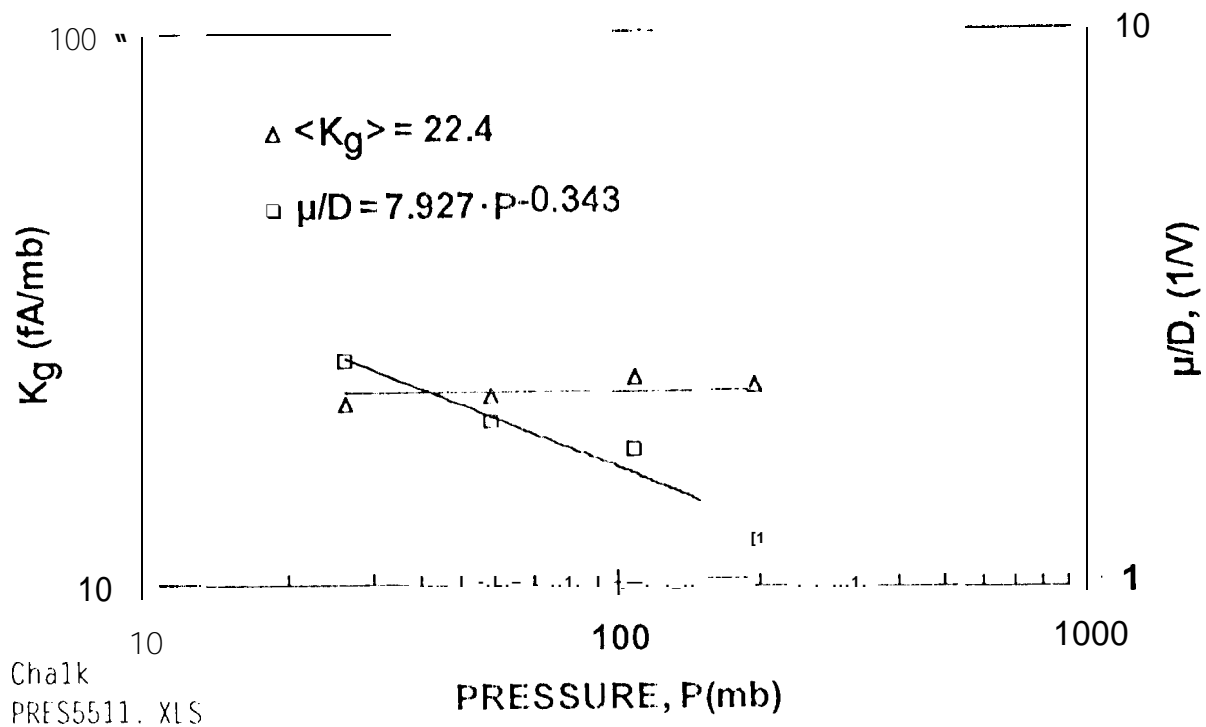


Figure 15. Current-voltage parameters, K_g and p/D , pressure dependence.

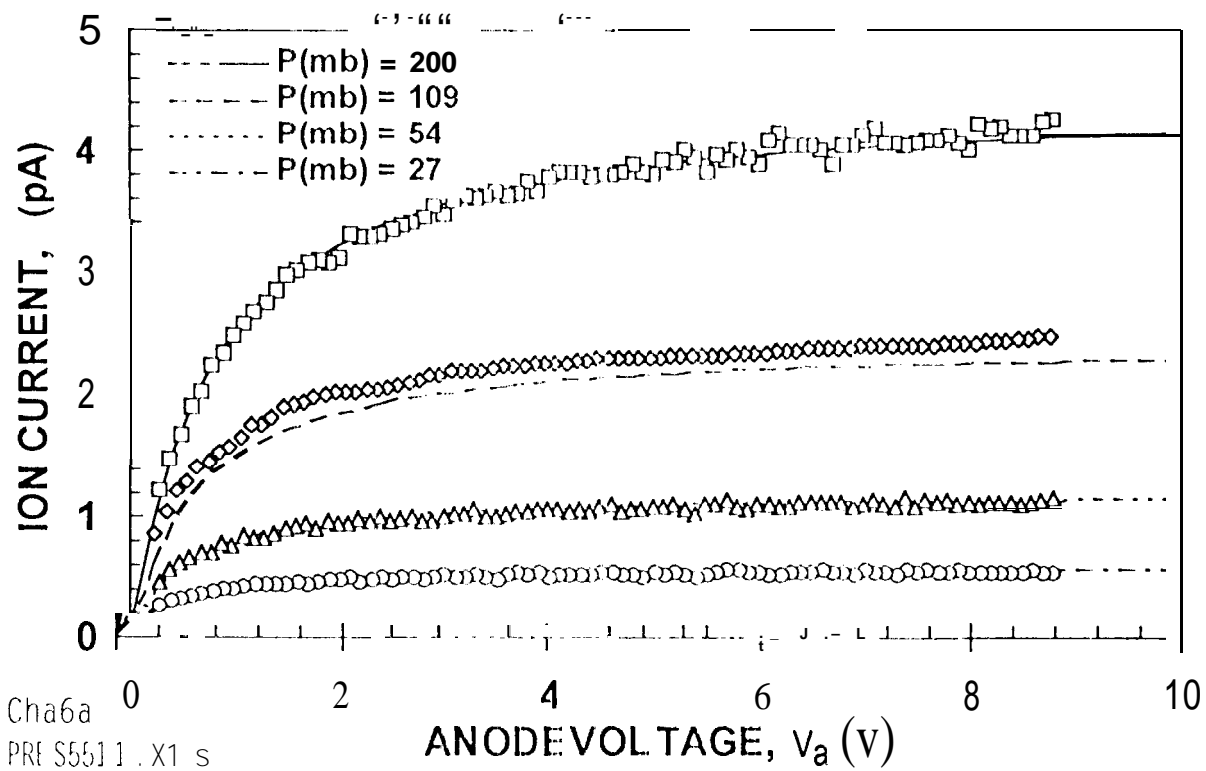


Figure 16. Experimental values (data points) from Fig. 9 compared to Eq. 30 (lines).

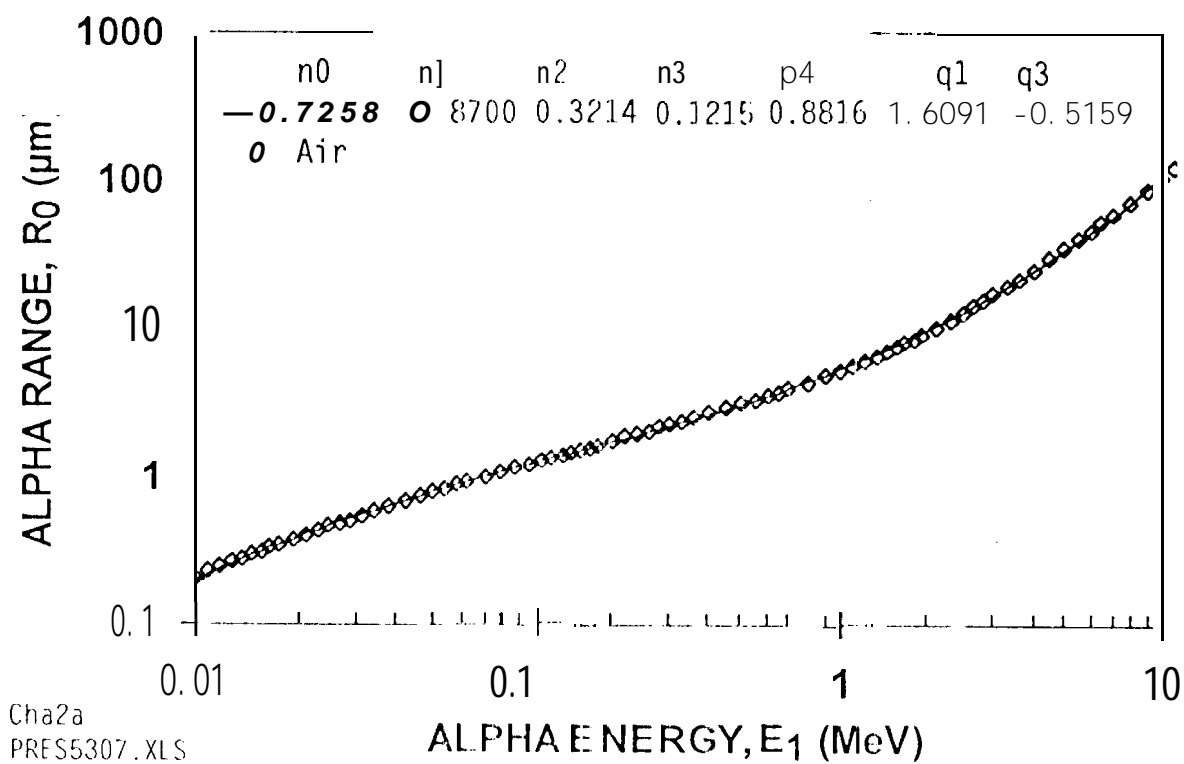


Figure 17. Cubic fit to the alpha particle range-energy curves in air at STP